Journal of Solid State Chemistry **165,** 345–358 (2002)
doi:10.1006/jssc.2002.9550, available online at http://www.idealibrary.com on IDEAL®

Analysis of the Electron Localization, the Anisotropy of Electrical Conductivity, the Orbital Ordering, and Spin-Exchange Interactions in $BaVS_3$ on the Basis of First Principles and Semi-empirical Electronic Structure Calculations

M.-H. Whangbo,[1] H.-J. Koo, and D. Dai

Department of Chemistry, North Carolina State University, Raleigh, North Carolina 27695-8204

and

A. Villesuzanne

ICMCB-CNRS, 87, avenue du Dr. A. Schweitzer, 33608 Pessac Cedex, France

Received November 20, 2001; in revised form February 05, 2002; accepted February 15, 2002

The electrical transport and magnetic properties of $BaVS_3$, made up of individual VS_3 octahedral chains, were examined on the basis of first principles and tight-binding electronic structure calculations. The electrical conductivity of $BaVS_3$ is nearly isotropic despite its one-dimensional structural feature, because of the orbital interactions associated with the short $S\cdots S$ contacts within each VS_3 chain and between adjacent VS_3 chains. The probable cause for the metal–insulator transition at ~ 70 K was examined in terms of first principles electronic structure calculations, which indicate that the metallic and magnetic insulating states of $BaVS_3$ are nearly the same in energy. This is consistent with the observation that the metal–insulator transition at ~ 70 K is caused by electron localization. The observed magnetic properties of $BaVS_3$ below ~ 70 K are readily explained under the assumption that the symmetry-broken t_{2g}-orbitals act as the magnetic orbitals in the magnetic insulating state of $BaVS_3$. The probable cause for the latter was discussed.

1. INTRODUCTION

In $BaVS_3$ face-sharing VS_6 octahedra form the VS_3 chains running along the c-axis, and the Ba^{2+} ions are located at the 12-coordination sites between three adjacent chains (Fig. 1) (1). This compound exhibits a number of interesting physical properties and as a result has received considerable attention (2–12). It undergoes three successive phase transitions at ~ 240, ~ 70 and ~ 30 K. At room temperature, $BaVS_3$ has the hexagonal perovskite-type structure, and the V^{4+} (d^1) ions in each VS_3 chain form a straight chain. Below ~ 240 K, it distorts into an orthorhombic structure in which the V^{4+} ions of each VS_3 chain show a zigzagging in a bc-plane with the $\angle$V–V–V angle of $\sim 160^\circ$ (Fig. 2) (2). $BaVS_3$ undergoes a metal–insulator transition at ~ 70 K; the electrical conductivity is nearly temperature independent above ~ 70 K and decreases sharply below ~ 70 K (6). $BaVS_3$ is a magnetic insulator below ~ 70 K (see below) and is a poor metal above ~ 70 K, which suggests that its metallic and magnetic insulating states are close in energy. If the coordinate z-direction is chosen along the chain direction (Fig. 3a), the V $3z^2–r^2$ orbital constitutes one of the t_{2g} levels of a VS_6 octahedron (Fig. 3b) (13). Intuitively, it is expected that the $3z^2–r^2$ orbitals give rise to stronger interactions between adjacent V^{4+} ions than do the remaining two t_{2g} orbitals (Fig. 3c and 3d), primarily along the chain than along the interchain directions. Thus $BaVS_3$ would be a one-dimensional (1D) metal. However, this expectation is not consistent with the experiment; the electrical conductivity along the chain is only several times larger than that along the interchain directions (6). This prompted the suggestion that the V $3z^2–r^2$ orbitals are not involved in the electron transport, and the band formed from the $3z^2–r^2$ orbitals does not overlap with the occupied states (6). However, the electronic band structure of $BaVS_3$ determined by first principles calculations (10) does not support this suggestion.

The magnetic structure of $BaVS_3$ is also intriguing. ^{51}V NMR and NQR measurements indicate that it has a non-magnetic ground state and a spin gap (5). These observations were interpreted in terms of an orbital

[1]To whom correspondence should be addressed. Fax: 919-515-7832. E-mail: whangbo@ncsu.edu.

0022-4596/02 $35.00

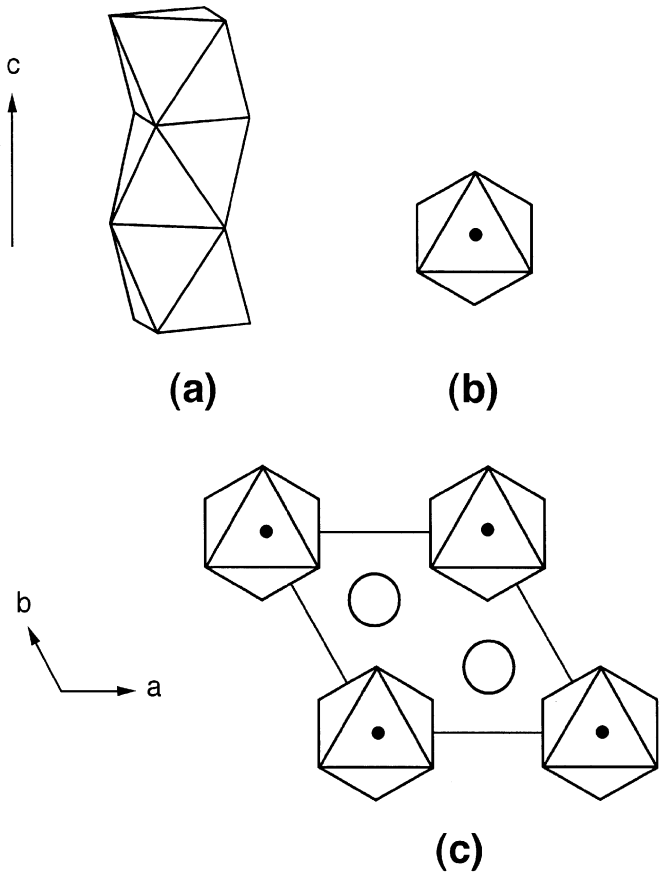

FIG. 1. Description of the crystal structure of $BaVS_3$: (a) perspective view of a VS_3 octahedral chain made up of face-sharing VS_6 octahedra in polyhedral representation; (b) projection view of a VS_3 chain along the chain direction, where the dot represents the position of the V atom; (c) projection view, along the c-direction, of the arrangements of the VS_3 chains, the V^{4+} ions (dots) and the Ba^{2+} ions (open circles) in the hexagonal structure of $BaVS_3$ at room temperature.

ordering in a spin-singlet state (5). The magnetic susceptibility of $BaVS_3$ shows a sharp peak at ~ 70 K and decreases rapidly below ~ 70 K (6). Such a temperature-dependent susceptibility is characteristic of an antiferromagnet. Indeed, the recent neutron diffraction study (7) found that $BaVS_3$ exhibits an incommensurate antiferromagnetic ordering with periodicity $\mathbf{q} = (0.226a^*, 0.226b^*, 0)$ below the temperature ~ 30 K. There is no long-range magnetic ordering between ~ 70 K and ~ 30 K, which is explained in terms of an orbital ordering in a spin-singlet state (5, 6). That the spins are ferromagnetically coupled along the chain direction (i.e., the c^* component of $\mathbf{q}$ is zero) below ~ 30 K is supported by the observations that the magnetic susceptibility has a positive Weiss temperature (3, 11), and the inelastic neutron scattering measurements show no antiferromagnetic intrachain coupling (12). The spin-exchange interaction between two adjacent spin sites in a magnetic solid is described by the spin-exchange parameter $J = J_F + J_{AF}$ (14–17). The antiferromagnetic term J_{AF} (<0) increases in magnitude as the overlap integral between the magnetic orbitals of the two spin sites is increased. The ferromagnetic term J_F (>0) is related to the overlap electron density between the magnetic orbitals (14) and is generally small. In general, the spin-exchange interaction becomes ferromagnetic (i.e., $J > 0$) when the J_{AF} term is small in magnitude. Consequently, the observed magnetic structure of $BaVS_3$ below ~ 30 K implies that the magnetic orbitals of the V^{4+} sites overlap more strongly along the interchain directions than along the intrachain direction, and that the interchain overlap between the magnetic orbitals is stronger along the $(a + b)$-direction than along the a- and b-direction of the low-temperature orthorhombic structure.

Thus, the electrical transport as well as the magnetic properties of $BaVS_3$ suggest that the metallic and magnetic insulating states of $BaVS_3$ are close in energy, that the intrachain interactions do not dominate over the interchain interactions in the energy levels around the Fermi level, and that in the magnetic insulating state the interchain antiferromagnetic spin-exchange interactions have one-dimensional character. The present work investigates the causes for these observations on the basis of both first principles and semi-empirical electronic structure calculations. Our work is organized as follows: the relative stabilities of the metallic and magnetic insulating states of $BaVS_3$ are estimated in Section 2 using first principles molecular electronic

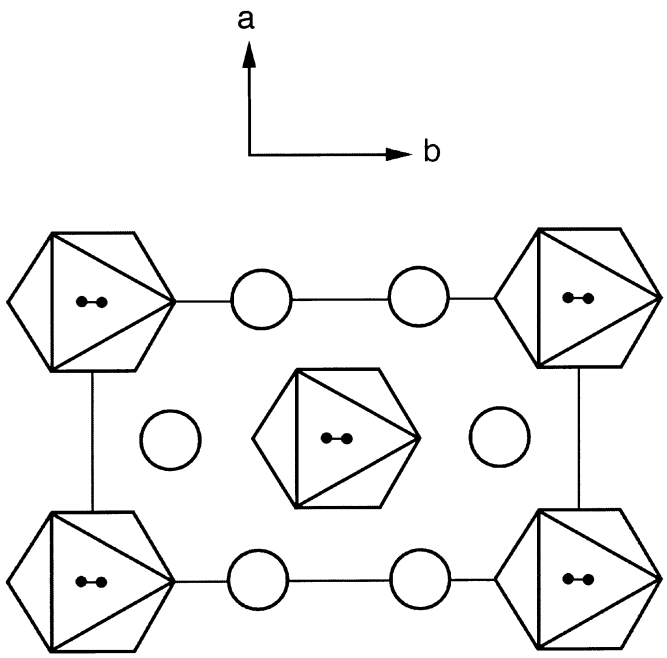

FIG. 2. Projection view, along the c-direction, of the arrangements of the VS_3 chains, the V^{4+} ions (dots) and the Ba^{2+} ions (open circles) in the orthorhombic structure of $BaVS_3$ below ~ 240 K. The zigzagging of the vanadium atoms occurs in a bc-plane.

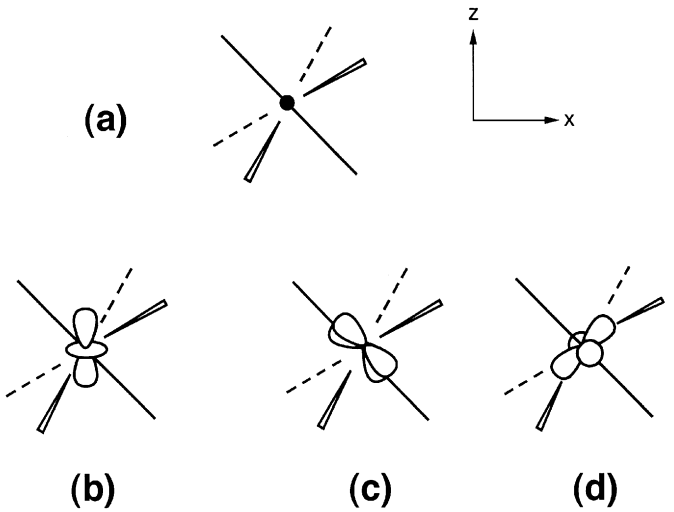

FIG. 3. (a) Local cartesian coordinate of a VS_6 octahedron, in which the z-axis is taken along the three-fold axis of the octahedron; d-orbitals contributing to the "symmetry-adapted" t_{2g}-orbitals of a VS_6 octahedron. These d-orbitals are $3z^2$–r^2 in (b), $\sqrt{2/3}xy - \sqrt{1/3}yz$ in (c), and $-\sqrt{2/3}(x^2 - y^2) - \sqrt{1/3}xz$ in (d).

structure calculations. Section 3 analyzes the nature of the energy levels of $BaVS_3$ around the Fermi level on the basis of semi-empirical electronic band structure calculations. The orbital ordering and spin-exchange interactions of $BaVS_3$ below ~ 70 K are discussed in Section 4 in terms of orbital interactions. Finally, our conclusions are summarized in Section 5. It should be noticed that first principles electronic structure calculations have the advantage of producing quantitative results, while semi-empirical tight-binding calculations facilitate the interpretation of computational results from the viewpoints of simple chemical concepts such as overlap, symmetry and electronegativity. Thus, a combined use of first principles and semi-empirical calculations allows one to gain insight into the question of what qualitative factors are critical in understanding quantitative computational results.

2. RELATIVE STABILITIES OF THE METALLIC AND MAGNETIC INSULATING STATES

The relative stabilities of the metallic and magnetic states of $BaVS_3$ can be estimated on the basis of first principles electronic structure calculations in two ways, i.e., electronic band structure calculations for the three-dimensional (3D) lattice of $BaVS_3$ and electronic structure calculations for a dimer unit of an isolated VS_3 octahedral chain. The latter approach assumes that the relative stabilities of the metallic and magnetic insulating states of the 3D lattice of $BaVS_3$ are well approximated by those of an individual VS_3 octahedral chain.

2.1. Dimer Electronic Structure Calculations

Consider a dimer unit of a 1D chain in which each site has one electron and one orbital (Fig. 4a). The orbital interaction between the two sites leads to the bonding and the antibonding levels (ϕ_1 and ϕ_2, respectively), which are separated by the energy Δe. The low-spin state $(\phi_1)^2$ (Fig. 4b) is more stable than the high-spin state $(\phi_1)^1(\phi_2)^1$ (Fig. 4c) if $U < 2\Delta e$, and the opposite is true if $U > 2\Delta e$ (18), where U is the on-site repulsion. The 1D chain with one electron and one orbital per site has a half-filled band. This chain can be metallic or magnetic insulating. From the viewpoint of band picture, the metallic state is related to the low-spin state of the dimer (Fig. 4d), and the magnetic insulating state to the high-spin state (Fig. 4e) (18). The metallic state is more stable than the magnetic insulating state if $U < 2\Delta e$, and the opposite is the case if $U > 2\Delta e$ (18). This is the same as the Mott–Hubbard criterion (19) because the bandwidth W for the 1D chain is equal to $2\Delta e$. Therefore, the relative stabilities of the metallic and the magnetic insulating states of an isolated VS_3 octahedral chain can be estimated by considering those of the low- and high-spin states of its dimer unit, i.e., the $(V_2S_9)^{10-}$ cluster (Fig. 5a) that consists of two V^{4+} and nine S^{2-} ions. To make electronic structure calculations reach self-consistent-field convergence, we reduce the negative charge of this cluster by replacing its outer six

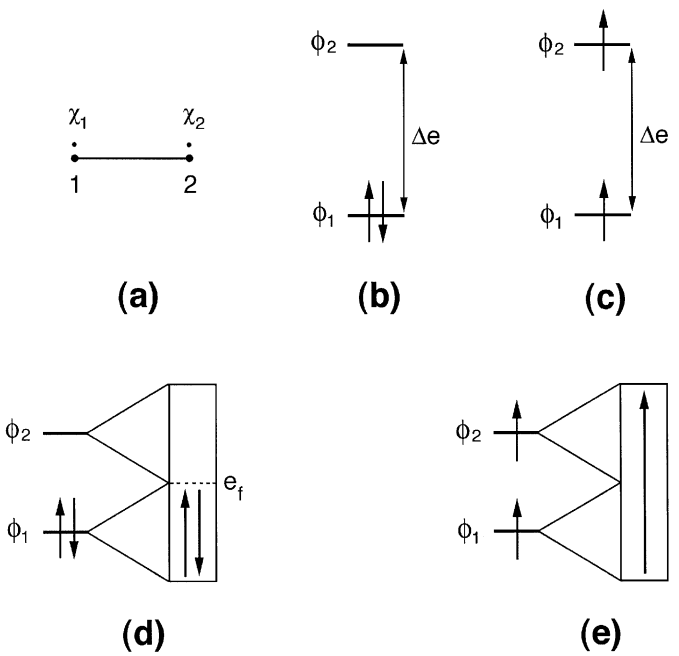

FIG. 4. (a) Dimer made up of two equivalent sites 1 and 2, where each site has one electron and one orbital; (b) low-spin state $(\phi_1)^2$ of a dimer; (c) high-spin state $(\phi_1)^1(\phi_2)^1$ of a dimer. The relationship between the low-spin state of a dimer and the metallic state of a chain in (d), and that between the high-spin state of a dimer and the magnetic insulating state of a chain in (e).

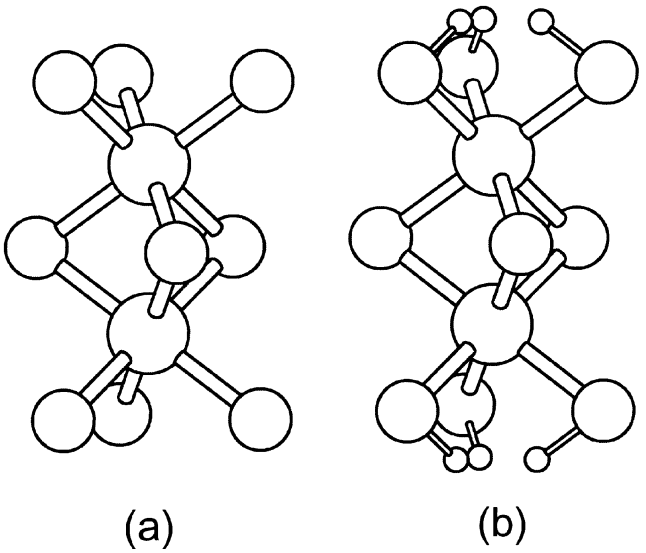

FIG. 5. Molecular clusters representing a dimer unit of an isolated VS_3 octahedral chain of $BaVS_3$. The $(V_2S_9)^{10-}$ cluster in (a), and the $(V_2S_9H_6)^{4-}$ cluster in (b).

S^{2-} ions with six $(SH)^-$ ions to form the $(V_2S_9H_6)^{4-}$ cluster (Fig. 5b), where the S–H bonds (1.40 Å) are pointed towards the missing V^{4+} sites of the VS_3 octahedral chain.

As presented in Fig. 6, the t_{2g}-levels of the two V^{4+} sites of the dimer $(V_2S_9H_6)^{4-}$ interact to give the six t_{2g}-block

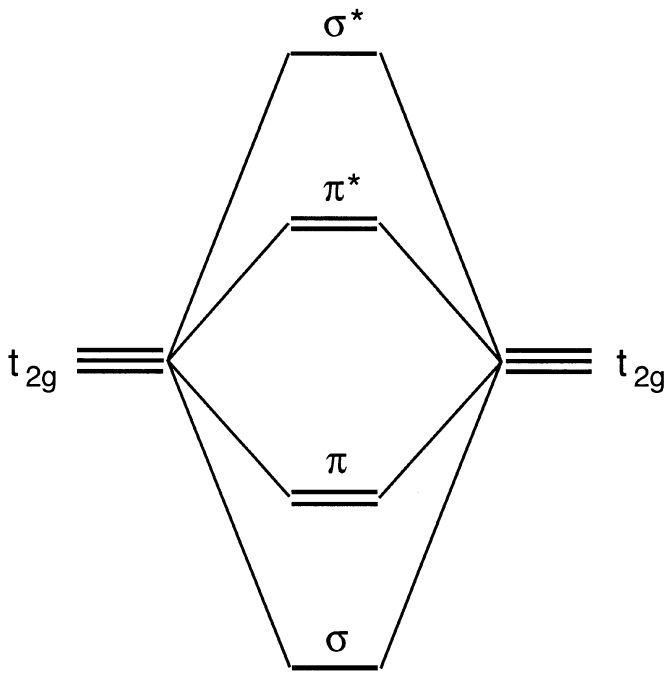

FIG. 6. Formation of the t_{2g}-block energy levels expected for the low-spin state of a dimer unit of an isolated VS_3 octahedral chain from the interactions between the $2t_{2g}$-levels of the two V^{4+} sites.

TABLE 1
Energies (in eV) Calculated for the Three States Φ_1, Φ_2 and Φ_3, of the Dimer Units, $(V_2S_9H_6)^{4-}$, Constructed from the Four Crystal Structures of $BaVS_3$[a, b]

	States		
Temperature	Φ_1	Φ_2	Φ_3
Room temperature (K)	− 62.26 (0.00)	− 62.11 (0.15)	− 61.41 (0.85)
100	− 62.18 (0.00)	− 62.05 (0.13)	− 61.33 (0.85)
60	− 62.20 (0.00)	− 62.09 (0.11)	− 61.38 (0.82)
5	− 62.12 (0.00)	− 61.98 (0.14)	− 61.25 (0.87)

[a]For each state, the energy listed is equal to the energy of the dimer unit minus the energies of the constituent atoms.

[b]The numbers in parentheses are the relative energies with respect to the low-spin state.

levels. The σ-bonding and σ^*-antibonding levels are derived from the $3z^2-r^2$ orbitals of the two V^{4+} sites (Fig. 3b), and the π-bonding and the π^*-antibonding levels from the remaining t_{2g}-levels of two V^{4+} sites (Fig. 3c and 3d). The electronic configurations relevant for our discussion are the low-spin state Φ_1 and the high-spin states Φ_2 and Φ_3:

$$\begin{aligned} \Phi_1 &= (\sigma)^2, \\ \Phi_2 &= (\sigma)^1(\pi)^1, \\ \Phi_3 &= (\pi)^2, \end{aligned} \qquad [1]$$

where all the filled levels lying below the *d*-block levels are suppressed for simplicity. To estimate the relative energies of these states, we carry out first principles density functional theory (DFT) calculations for the dimer $(V_2S_9H_6)^{4-}$ using the Amsterdam Density Functional program package (20). We employ spin-restricted calculations for the low-spin state Φ_1 and spin unrestricted calculations for the high-spin states Φ_2 and Φ_3 using the V 4*s*/4*p*/3*d*, S 3*s*/3*p* orbitals and H 1*s* orbital as valence shells with the remaining orbitals frozen in the cores. In our calculations the triple-zeta Slater-type orbitals (STO) plus polarization functions of the ADF package are used, and the Vosko–Wilk–Nusair (21), Becke88 (22) and Perdew86 (23) functions are chosen as the local-density-approximation (LDA), gradient-exchange and gradient-correlation functionals, respectively.

Table 1 summarizes the energies of the three states calculated for the dimer units constructed from the room temperature, 100, 60 and 5 K crystal structures of $BaVS_3$ (2). For each dimer unit, the low-spin state Φ_1 is most stable, the high-spin state Φ_2 is very close in energy to the low-spin state Φ_1, and the high-spin state Φ_3 is slightly less stable than the low-spin state Φ_1. In the low-spin state Φ_1 of the dimer for the room temperature structure of $BaVS_3$, the σ- and σ^*-levels are separated by 1.48 eV, the π- and π^*-levels

by 0.30 eV, and the σ- and π-levels by 0.64 eV. Thus the energy difference between the high-spin states Φ_2 and Φ_3 mainly reflects the energy difference between the σ- and π-levels. The same trend is observed for the dimers constructed from the 100, 60 and 5 K crystal structures of $BaVS_3$.

It is noted that in DFT calculations, the electronic structure of a system with strong electron correlation (e.g., a magnetic solid) is not well described. Currently, this deficiency in first principles electronic band structure calculations is corrected empirically by using the LDA + U method (24). The extent of on-site repulsion U is greater in the low-spin state Φ_1 than in the high-spin states Φ_2 and Φ_3, and the on-site repulsion has the effect of raising the energy of the low-spin state with respect to the high-spin states. Thus the high-spin state Φ_2 might even become more stable than the low-spin state. In any event, it is clear that the metallic and the magnetic insulating states of an isolated VS_3 octahedral chain are very close in energy. This in turn suggests that the metallic and the magnetic insulating states of $BaVS_3$ would be similar in energy.

2.2. *Electronic Band Structure Calculations*

First principles full potential linearized augmented plane wave (FP-LAPW) calculations (25) were carried out for the room-temperature structure of $BaVS_3$ using the WIEN97 program package within the generalized gradient approximation (26) for the exchange-correlation energy. We employed the muffin-tin radii of 2.5 a.u. for Ba, 2.4 a.u. for V and 2.1 a.u. for S. The basis set cut-off parameters were $G_{max} = 10$ and $RK_{max} = 8$. Integrations over the irreducible wedge of the Brillouin zone were performed using a 72 k-points regular mesh. To estimate the relative stability of the metallic and magnetic insulating states of $BaVS_3$, the normal metallic and the ferromagnetic metallic states were studied by non-spin- and spin-polarized electronic band structure calculations, respectively.

Results of our non-spin-polarized calculations are summarized in Fig. 7a and 7b. The band dispersion relations of Fig. 7a are quite similar to those reported in Ref. (10), and show that the Fermi level crosses the $3z^2$–r^2 band that is approximately 2 eV wide. Namely, the states around the Fermi level do have contributions from the V $3z^2$–r^2 orbitals. In the partial density of states (DOS) plot for the $3z^2$–r^2 orbital (Fig. 7b), more states are found above than below the Fermi level; the $3z^2$–r^2 band is less than a quarter filled. A sharp DOS peak is present very close to the Fermi level. The narrow bands leading to this peak result essentially from the t_{2g} levels of Fig. 3c and 3d. When a normal metallic state has the Fermi level very close to a sharp DOS peak, an alternative electronic state with localized electrons can become more stable.

Results of our spin-polarized calculations are summarized in Fig. 8 for the up-spin bands, and in Fig. 9 for the down-spin bands. The up-spin bands exhibit electronic features very similar to those found for the non-spin-polarized calculations and have the Fermi level at the sharp DOS

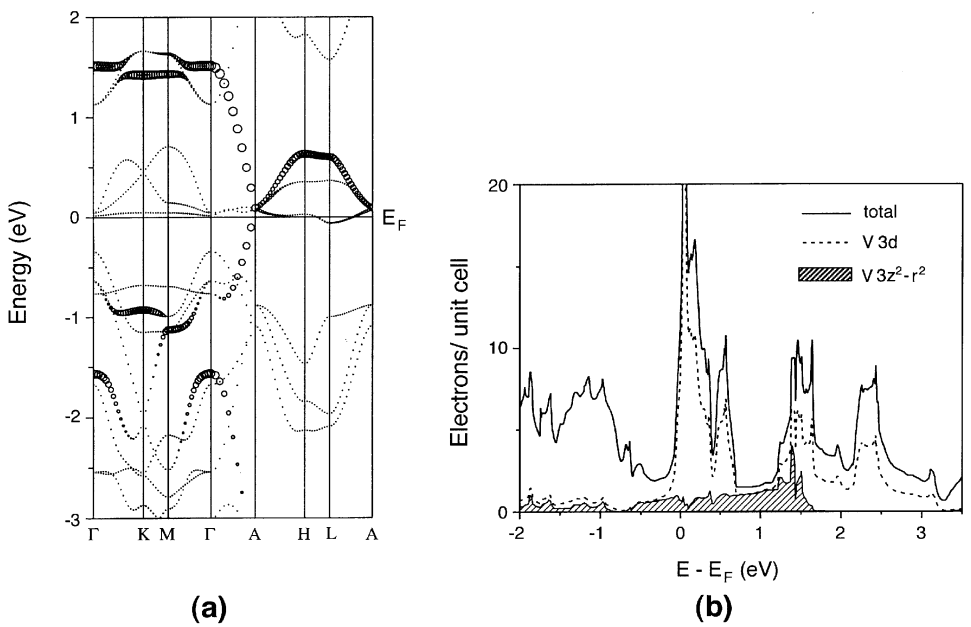

FIG. 7. Band structure of $BaVS_3$ calculated for the normal metallic state by non-spin-polarized FP-LAPW calculations. (a) band dispersion relations, where the $3z^2$–r^2 orbital contributions are given by fat band representations; (b) total and partial DOS plots. In (a) the wave vector points are defined as follows: $\Gamma = (0, 0, 0)$, $M = (a^*/2, 0, 0)$, $K = (a^*/3, b^*/3, 0)$, $A = (0, 0, c^*/2)$, $L = (a^*/2, 0, c^*/2)$ and $H = (a^*/3, b^*/3, c^*/2)$.

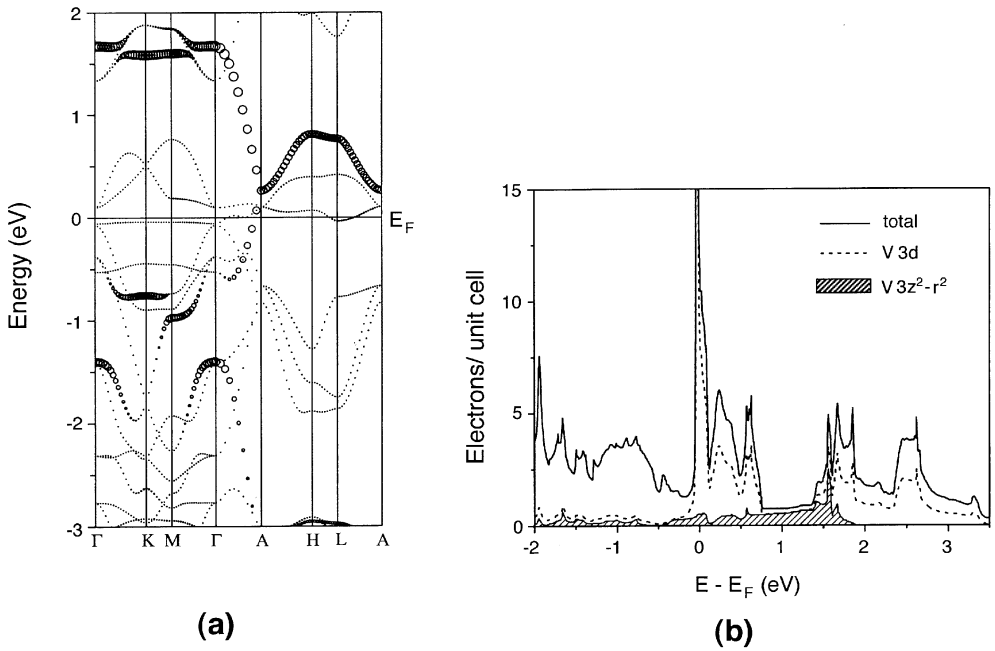

FIG. 8. Up-spin band structure of $BaVS_3$ calculated for the ferromagnetic metallic state by spin-polarized FP-LAPW calculations. (a) dispersion relations, where the $3z^2–r^2$ orbital contributions are represented by fat bands; (b) total and partial DOS plots.

peak. The latter means that the t_{2g}-block levels of the VS_6 octahedra contributing to the sharp DOS peak interact weakly. Thus, it is likely that the electrons in these orbitals are localized. With respect to the *d*-block bands of the up-spin bands, those of the down-spin bands are raised in energy. In both spin-polarized and non-spin-polarized calculations, the bottom portion of the $3z^2–r^2$ band is only slightly occupied. The only noticeable change for the $3z^2–r^2$ orbitals is an increase of band width for down spins with respect to the non-spin-polarized and up-spin cases.

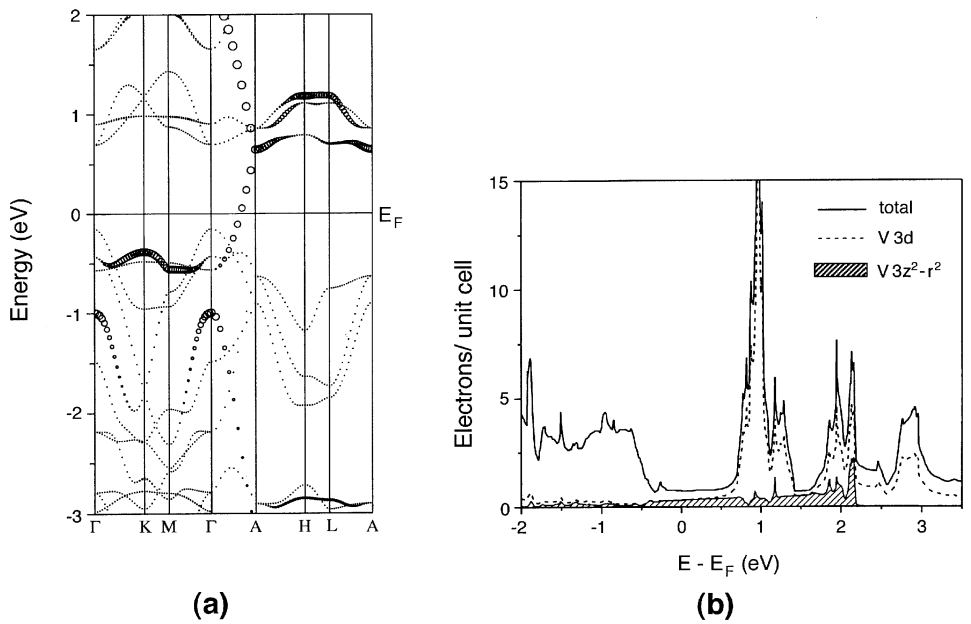

FIG. 9. Down-spin band structure of $BaVS_3$ calculated for the ferromagnetic metallic state by spin-polarized FP-LAPW calculations: (a) dispersion relations, where the $3z^2–r^2$ orbital contributions are represented by fat bands; (b) total and partial DOS plots.

In the ferromagnetic metallic state represented by the spin-polarized calculations, there is one unpaired spin per formula unit $BaVS_3$. Rigorously speaking, this state is not identical with the magnetic insulating state of $BaVS_3$ (27, 28). Nevertheless, the two states are similar in that both describe a state in which there is one localized electron per formula unit. Therefore, in comparing the relative stabilities, the metallic and magnetic insulating states of $BaVS_3$ can be approximated by the normal metallic and the ferromagnetic metallic states, respectively. Our FP-LAPW calculations reveal that these two states are practically the same in stability, i.e., the ferromagnetic metallic state is more stable than the normal metallic state only by 0.05 eV per formula unit. This conclusion is the same as that reached from the dimer electronic structure calculations.

3. NATURE OF THE BANDS AROUND THE FERMI LEVEL

Let us now examine the nature of the bands of $BaVS_3$ in the region of the Fermi level in some detail. For this purpose, we calculate the electronic band structure for the room temperature structure of $BaVS_3$ using the extended Hückel tight binding (EHTB) method (29, 30) and analyze the results from the viewpoint of orbital interactions.

In calculating the electronic structures of transition metal compounds using the EHTB method, it has been conventional to represent the *d* orbitals of transition metal elements by double-zeta (DZ) STOs (31), and the *s*/*p* orbitals of main group elements by single-zeta (SZ) STOs. This "DZ/SZ" calculation is useful in highlighting the splitting patterns of the *d*-block levels in discrete molecules. However, this calculation underestimates the magnitudes of interactions between main group elements in short contacts and hence can lead to a misleading result for an extended solid if such short contacts occur continuously throughout the solid lattice. For the most antibonding level formed from the main group *p* orbitals may rise above the bottom of the *d*-block levels. In such a case, it is necessary to use DZ STOs not only for the *d* orbitals of the transition metal but also for the *s*/*p* orbitals of the main group elements. We carry out this "DZ/DZ" calculation as well as the "DZ/SZ" calculation for the electronic structure of $BaVS_3$ using the room temperature crystal structure. The parameters of the atomic orbitals used for our DZ/SZ and DZ/DZ calculations are listed in Table 2.

The electronic band structure of $BaVS_3$ obtained from DZ/SZ calculations is summarized in Fig. 10. The density of state (DOS) plot in Fig. 10a shows that the t_{2g}-block bands are separated from the *p*-block bands lying below and also from the e_g-block bands lying above. The dispersion relations of the t_{2g}-block bands are presented in Fig. 10b, where the wide band resulting from the $3z^2-r^2$ orbitals is dispersive

TABLE 2

Exponents ζ_i and Valence Shell Ionization Potentials H_{ii} of Slater-Type Orbitals χ_i Used for Extended Hückel Tight-Binding Calculation[a]

Atom	χ_i	H_{ii} (eV)	ζ_1	c_1[b]	ζ_2	c_2[b]
V	4*s*	−8.81	1.697	1.0		
V	4*p*	−5.52	1.260	1.0		
V	3*d*	−11.0	5.025	0.3738	2.173	0.7456
S	3*s*	−20.0	2.121	1.0		
S	3*p*	−13.3	1.827	1.0		
S	3*s*	−20.0	2.622	0.5990	1.688	0.5246
S	3*p*	−13.3	2.338	0.5377	1.333	0.5615

[a] H_{ii}'s are the diagonal matrix elements $\langle\chi_i|H^{\text{eff}}|\chi_i\rangle$, where H^{eff} is the effective Hamiltonian. In our calculations of the off-diagonal matrix elements $H^{\text{eff}} = \langle\chi_i|H^{\text{eff}}|\chi_i\rangle$, the weighted formula was used. See: J. Ammeter, H.-B. Bürgi, J. Thibeault, and R. Hoffmann, *J. Am. Chem. Soc.* **100,** 3686 (1978).

[b] Coefficients used in the double-zeta Slater-type orbital expansion.

mainly along the chain direction. Let us examine how this result changes by DZ/DZ calculations. The use of DZ STOs for S 3*p* enhances overlap between S atoms in short S ⋯ S contacts. The nearest-neighbor intrachain and interchain S ⋯ S contacts in the room temperature structure of $BaVS_3$ are 3.40 and 3.38 Å, respectively (2). In general, the interactions between non-bonded S ⋯ S contacts are regarded as negligible when the S ⋯ S contact distances are greater than the sum of the van der Waals radii (i.e., 3.2 Å) (32). However, the non-bonded interaction can be substantial for an S ⋯ S contact distance slightly longer than 3.2 Å if the crystal structure allows the S 3*p* orbitals to be aligned along or close to the S ⋯ S contact direction. In a DZ STO representation, the radial part of the S 3*p* orbital, $\chi_{3p}(r)$, is written as

$$\chi_{3p}(r) = r^2[c_1 \exp(-\zeta_1 r) + c_2 \exp(-\zeta_2 r)].$$

The exponents ζ_1 and ζ_2 describe contracted and diffuse STOs, respectively (i.e., $\zeta_1 > \zeta_2$). The diffuse STO provides an orbital tail that enhances overlap between S atoms in short S ⋯ S contacts. Such an overlap is enhanced as the ζ_2 value becomes smaller, but is reduced as ζ_2 becomes larger.

To facilitate the discussion of our DZ/DZ calculations, it is convenient to first examine how the diffuseness of the S 3*p* orbital affects the electronic band structure of an isolated VS_3 octahedral chain. Figs. 11a–11d show how the band structure of a VS_3 chain varies when the ζ_2 value of the S 3*p* orbital is gradually increased as $\zeta_2(1 + x)$, i.e., as the diffuseness of the S 3*p* orbital is decreased ($x \geq 0$). The band structures calculated for $x = 0.00$, 0.05, 0.10 and 0.15 are presented in Figs. 11a–11d, respectively. The two bands

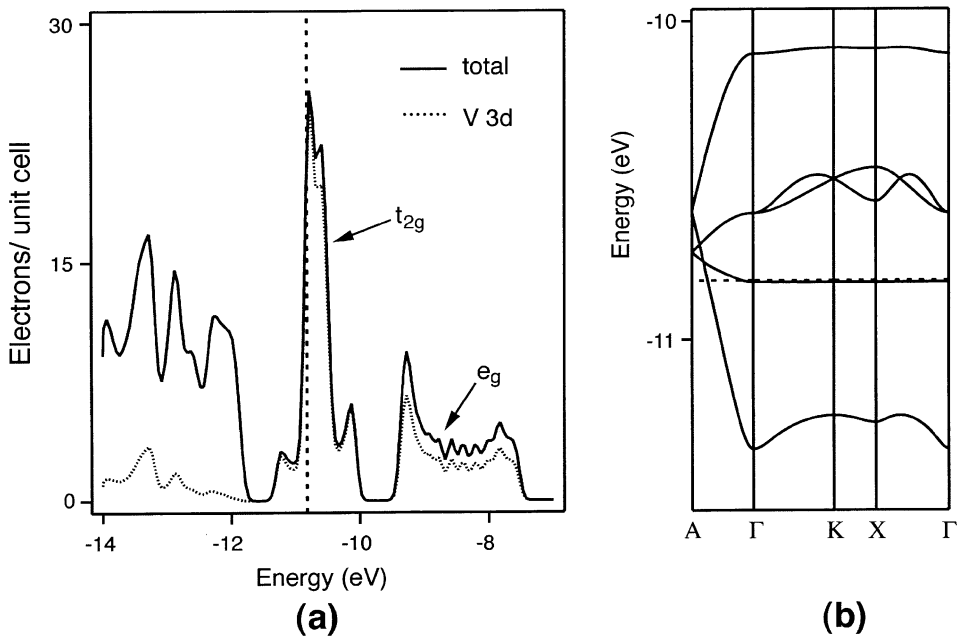

FIG. 10. Electronic band structure of $BaVS_3$ obtained by DZ/SZ calculations: (a) plots of the total DOS (solid line) and the partial DOS (dotted line) for the V 3d orbitals; (b) dispersion relations of the t_{2g}-block bands.

presented by bold lines are the σ-bands that depend sensitively on the diffuseness of the S $3p$ orbital. These bands result mainly from the V $3z^2$–r^2 and the S $3z$ orbitals. To explain their dispersion relations, we note that an isolated VS_3 octahedral chain has the V atoms and S_3 triangles alternate along the chain (Fig. 12a). The most antibonding and the most bonding combinations of the V $3z^2$–r^2 orbitals along the chain (hereafter referred to as the (z^2)* and (z^2) levels, respectively) are depicted in Figs. 12b and 12c, respectively. The π_z orbitals of S_3 triangles (Fig. 13a) also make σ-interactions along the chain. The most antibonding and the most bonding combinations of these π_z orbitals (hereafter referred to as the (z)* and (z) levels, respectively) are depicted in Figs. 12d and 12e, respectively, where each π_z orbital is represented by one z orbital for simplicity. An isolated VS_3 chain has two formula units per unit cell, so

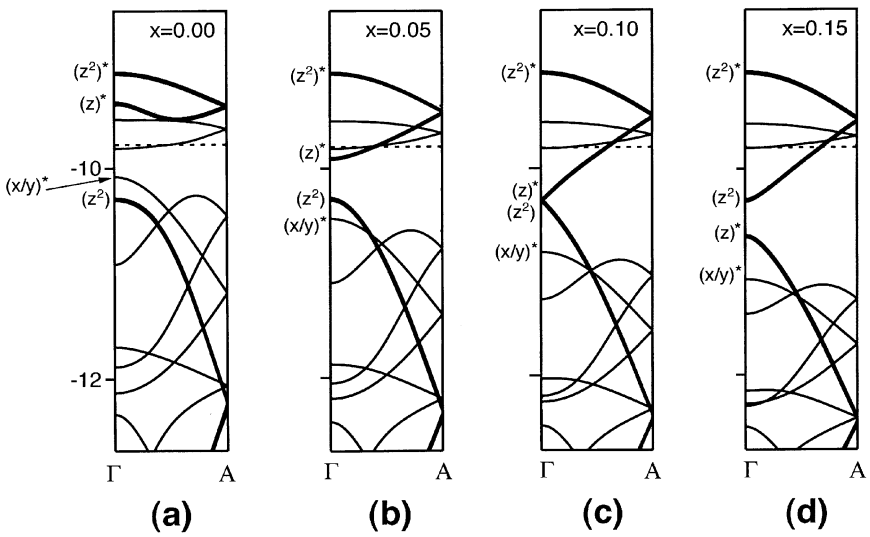

FIG. 11. Electronic band structures of an isolated VS_3 octahedral chain obtained from DZ/DZ calculations when the ζ_2 value of the S $3p$ orbital is gradually increased as $\zeta_2(1 + x)$: (a) $x = 0.00$; (b) $x = 0.05$; (c) $x = 0.10$; and (d) $x = 0.15$.

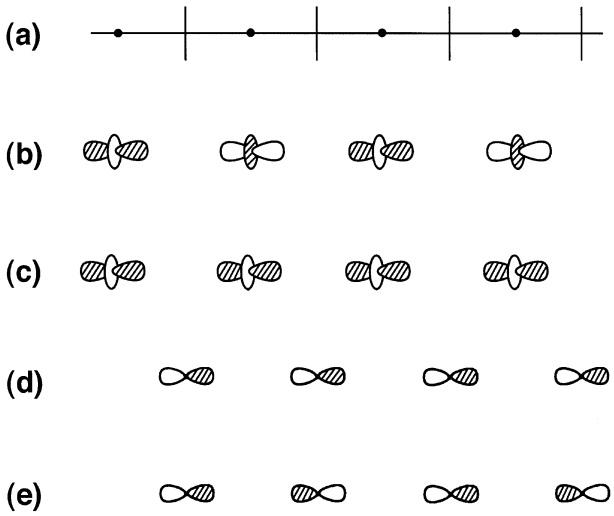

FIG. 12. (a) Schematic representation of an isolated VS_3 octahedral chain, where the dots represent the V atoms while the vertical line segments perpendicular to the chain represent the S_3 triangles; (b) most antibonding combination of the V $3z^2$–r^2 orbital, (z^2)*; (c) most bonding combination of the V $3z^2$–r^2 orbital, (z^2); (d) most antibonding combination of the π_z orbitals, (z)*; (e) most bonding combination of the π_z orbitals, (z).

that the (z^2), (z^2)*, (z) and (z)* levels occur at the Γ point. In Fig. 11d the (z^2) level lies higher than the (z)* level. As the diffuseness of the S $3p$ orbital increases (i.e., as x decreases), the (z)* level is raised in energy eventually rising above the (z^2) level (Figs. 11a and 11b). This has an important consequence on the major orbital composition of the higher-lying σ-band that is cut by the Fermi level. In Figs. 11a–11d the main orbital character of the top half of the higher-lying σ-band is the V $3z^2$–r^2 orbital. However, the main orbital character of the bottom half of the higher-lying σ-band changes gradually from the S_3 π_z orbital in Fig. 11a to the V $3z^2$–r^2 orbital in Fig. 11d. Thus, the V $3z^2$–r^2 orbital character is strong at the Fermi level in Fig. 11d, but weak in Fig. 11a.

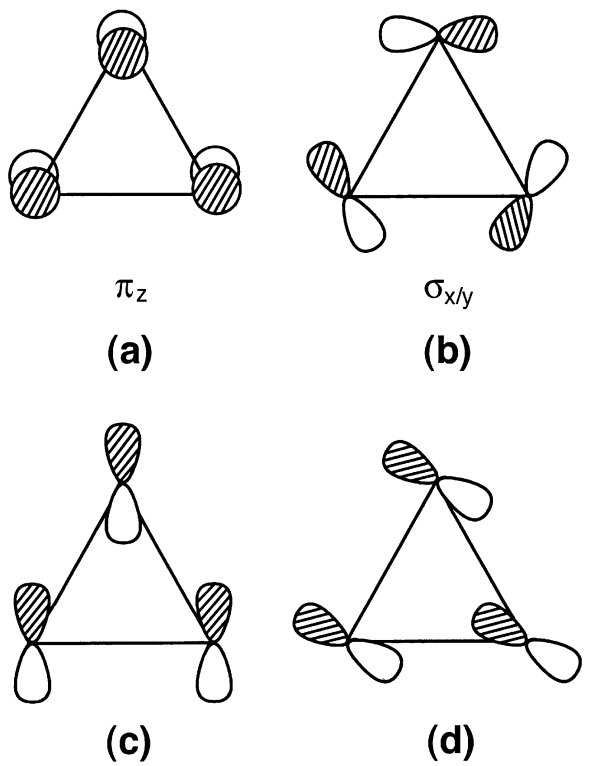

FIG. 13. Group orbitals of an S_3 triangle that are crucial for the interactions for the short intrachain S ⋯ S contacts in (a), and for the short interchain S ⋯ S contacts in (b–d).

We now examine the electronic band structure for the 3D lattice of $BaVS_3$ obtained by DZ/DZ calculations. In $BaVS_3$, the adjacent VS_3 chains interact via the short interchain S ⋯ S contacts. The group orbitals of an S_3 triangle important for these interchain interactions are the in-plane S $3p$ orbitals, one example of which is the $\sigma_{x/y}$ orbital shown in Fig. 13b. When the $\sigma_{x/y}$ orbitals of the S_3 triangles are combined out-of-phase along the chain, they lead to the level lying just below the (z) level at Γ, as indicated by the label (x/y)* in Figs. 11a–11d. The levels made up of other in-plane S $3p$ orbitals (e.g., see Figs. 13c and 13d) lie below the (x/y)* level. The interchain S ⋯ S interactions in $BaVS_3$ raise the p-block levels made up of the in-plane S $3p$ orbitals. Figs. 14a–14d show the band structures of $BaVS_3$ obtained from DZ/DZ calculations when the ζ_2 value of the S $3p$ orbital is gradually increased as $\zeta_2(1 + x)$. For $x = 0.00$, a comparison of Figs. 11a and 14a reveals that the (x/y)* level is raised above the (z^2)* level in the 3D lattice of $BaVS_3$. As the S $3p$ orbital is made to contract more (i.e., as x increases), the p-block levels made up of the in-plane S $3p$ orbitals are gradually lowered in energy such that in Fig. 14d the p-block bands do not overlap with the t_{2g}-block bands any more. Figs. 15a–15d show the DOS plots calculated for the energy region of the t_{2g}-block bands (corresponding to the band dispersion relations of Figs. 14a–14d, respectively). The V $3z^2$–r^2 orbital character at the Fermi level is negligibly small in Fig. 15a, but increases steadily as the S $3p$ orbital becomes more contracted. The EHTB band structure obtained for $x = 0.10$ (Fig. 15c) is close to the first principles electronic band structure of $BaVS_3$ calculated for its normal metallic state (Fig. 7).

4. ORBITAL INTERACTIONS AND ORBITAL ORDERING

In order to account for the spin ordering of $BaVS_3$ below ~70 K, we examine the spin-exchange interactions of $BaVS_3$ on the basis of spin dimer analysis in which the EHTB method is used to calculate spin-exchange interactions (15–17). This approach has been successful in explaining the spin-exchange interactions in various magnetic solids when spin-orbital interaction energies (see below) are obtained using DZ/DZ calculations (15–17).

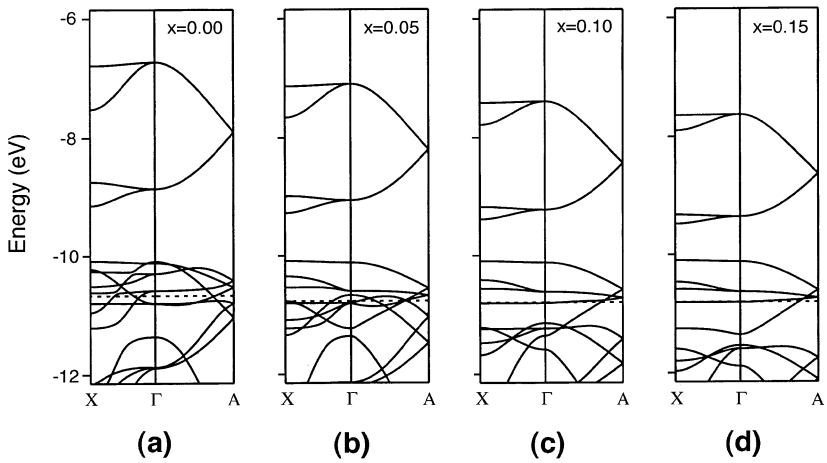

FIG. 14. Electronic band structures of $BaVS_3$ obtained from DZ/DZ calculations when the ζ_2 value of the S 3*p* orbital is gradually increased as $\zeta_2(1 + x)$: (a) $x = 0.00$; (b) $x = 0.05$; (c) $x = 0.10$; and (d) $x = 0.15$.

For the local coordinate system of a VS_6 octahedron in Fig. 3a, the t_{2g}-orbitals are given as shown in Figs. 3b–3d. For the convenience of our discussion, these orbitals will be referred to as the "symmetry-adapted" t_{2g}-orbitals. When the local coordinate system of a VS_6 octahedron is chosen as in Fig. 16a, we obtain the t_{2g}-orbitals presented in Figs. 16b–16d, which will be referred to as the "symmetry-broken" t_{2g}-orbitals. The latter have been found useful in describing electronic instabilities such as charge density wave in layered transition metal dichalcogenides

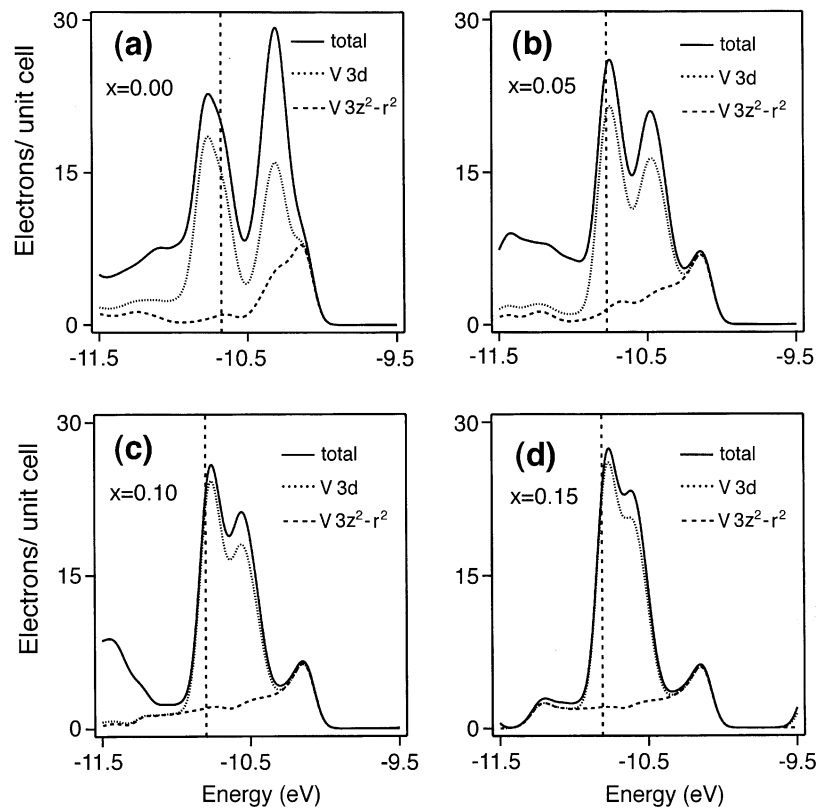

FIG. 15. Total and partial DOS plots of $BaVS_3$ obtained from DZ/DZ calculations when the ζ_2 value of the S 3*p* orbital is gradually increased as $\zeta_2(1 + x)$: (a) $x = 0.00$; (b) $x = 0.05$; (c) $x = 0.10$; and (d) $x = 0.15$.

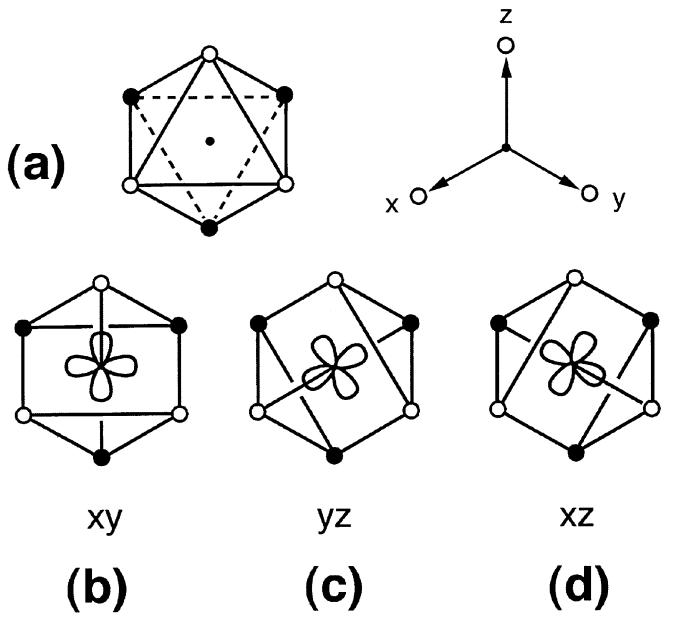

FIG. 16. (a) Alternative choice of the local cartesian coordinate for a VS_6 octahedron; *d*-orbitals contributing to the "symmetry-broken" t_{2g}-block levels of a VS_6 octahedron. These *d*-orbitals are described by *xy* in (b), *yz* in (c), and *xz* in (d).

MQ_2 (33, 34). In the orthorhombic structures of $BaVS_3$, nearest-neighbor "interchain" interactions involving the "symmetry-broken" t_{2g}-orbitals occur along the $(a + b)$-direction (Fig. 17a), the *a*-direction (Fig. 17b), and the $(-a + b)$-direction (not shown). Such interactions do not occur along the *b*-direction. For simplicity, only the "equatorial" planes containing the "symmetry-broken" t_{2g}-orbitals are shown in Figs. 17a and 17b. The interaction along the $(-a + b)$-direction, which involves the "symmetry-broken" t_{2g}-orbital not employed in Figs. 17a and 17b, is equivalent to that along the $(a + b)$-direction. As depicted in Fig. 17c, the t_{2g}-orbitals contained in the "equatorial" planes (when singly occupied) give rise to a super–super exchange (V–S $\cdots$ S–V) interaction, which occurs via the overlap between the S 3*p* orbital tails (15–17). The interchain spin-exchange interactions in $BaVS_3$ should take place through such super–super exchange interactions. In principle, the interchain spin-exchange interaction of any given V^{4+} site may take place along the $(a + b)$-, $(-a + b)$- or *a*-direction. If such interactions occur randomly in each plane of VS_6 octahedra parallel to the *ab*-plane (e.g., see Fig. 18), then there will be no long-range magnetic ordering although spins are all paired up via nearest-neighbor interchain spin-exchange interactions (5, 6). Such a state would describe the magnetic structure of $BaVS_3$ between ~ 70 and ~ 30 K.

Let us estimate the relative strengths of the intrachain and interchain spin-exchange interactions in $BaVS_3$. Suppose that the two spin sites of a spin dimer (i.e., a structural unit containing two spin sites, as shown in Fig. 4a) are described by the non-orthogonal magnetic orbitals χ_1 and χ_2, S_{12} is the overlap integral between χ_1 and χ_2, and Δe is the spin-orbital interaction energy (Fig. 4c). Then the antiferromagnetic spin-exchange parameter J_{AF} (< 0) of the spin dimer depends on S_{12} and Δe as $J_{AF} \propto -(S_{12})^2 \propto -(\Delta e)^2$. When the magnetic orbitals of $BaVS_3$ are given by the symmetry-broken t_{2g}-orbitals, the Δe value for the *interchain* spin-exchange interaction, Δe_{inter}, is easily calculated by performing molecular orbital calculations for the appropriate spin dimer $(V_2S_{12})^{16-}$ that consists of two $(VS_6)^{8-}$ octahedra (Figs. 17a and 17b). However, it is not straightforward to evaluate the Δe value for the *intrachain*

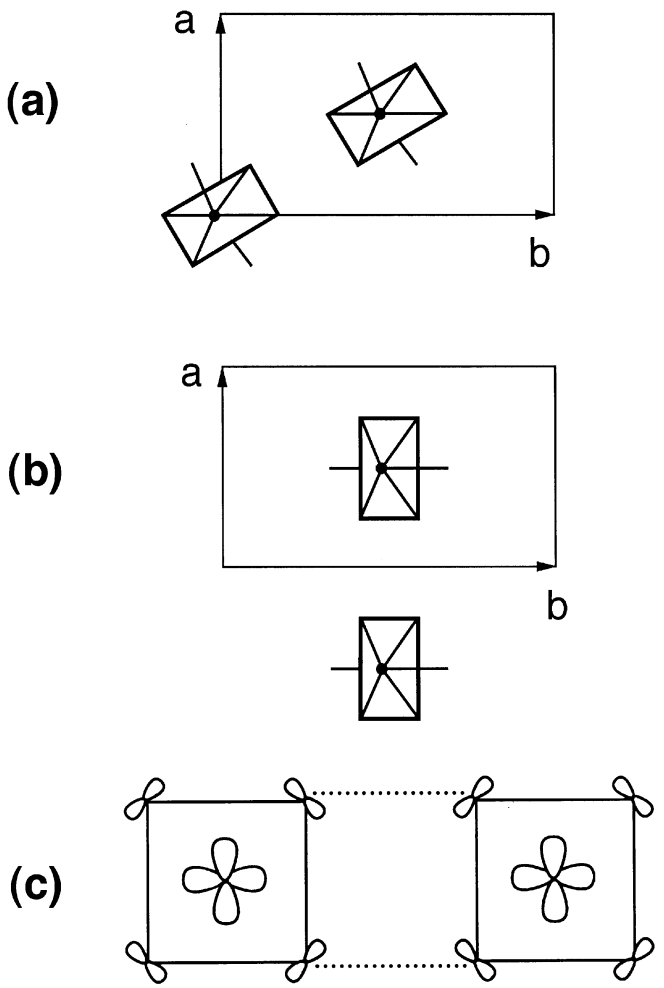

FIG. 17. (a) Arrangement of the "equatorial" planes containing the "symmetry-broken" t_{2g}-orbitals along the $(a + b)$-direction, and (b) that along the *a*-direction, in the orthorhombic structure of $BaVS_3$. For simplicity, the "symmetry-broken" t_{2g}-orbitals contained in the "equatorial" planes are not shown. The $(a + b)$- and $(-a + b)$-directions are equivalent by symmetry. (c) Overlap between the S 3*p* orbital tails of the magnetic orbitals contained in the "equatorial" planes of (a) and (b). The overlap leads to super–super exchange (V–S $\cdots$ S–V) interactions.

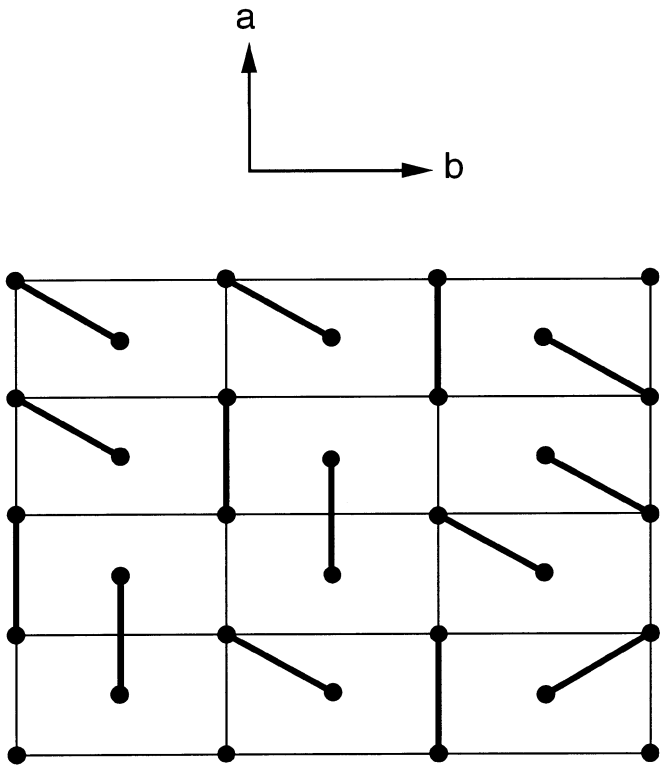

FIG. 18. Random arrangement of antiferromagnetically coupled interchain spin dimers (represented by solid lines) within a layer of VS_6 octahedra parallel to the *ab*-plane. The dots represent the V^{4+} ion positions.

spin-exchange interaction, Δe_{intra}, which is a super-exchange (V–S–V) interaction. This intrachain spin-exchange interaction can occur via a shared corner (Fig. 19b) or a shared edge (Fig. 19c). In both cases, the two magnetic orbitals involved are not contained in the same plane, so that the associated Δe_{intra} values are expected to be small.

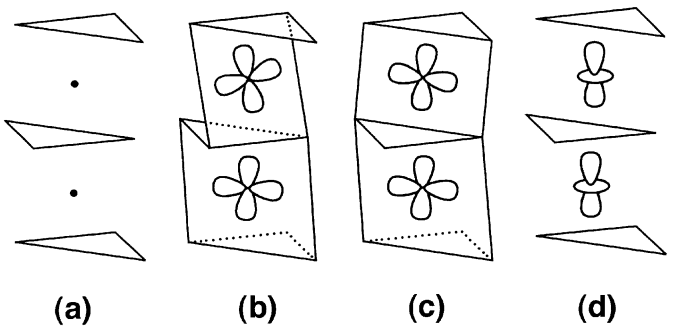

FIG. 19. (a) Schematic representation of the intrachain spin dimer unit $(V_2S_9)^{10-}$. The dots represent the V^{4+} ions, and the triangles the S_3 triangles; (b) two symmetry-broken t_{2g}-orbitals in a corner-sharing square planar units; (c) two symmetry-broken t_{2g}-orbitals in an edge-sharing square planar units; (d) two symmetry-adapted $3z^2-r^2$ orbitals interacting through the shared face.

The Δe_{intra} value can be estimated indirectly. The two spin sites of a spin dimer in $BaVS_3$ have V^{4+} (d^1) ions. Thus at each spin site one of the three t_{2g}-orbitals (ξ_1, ξ_2 and ξ_3) is singly occupied. The $(t_{2g})^1$ state of a V^{4+} (d^1) ion is described by the configurations $(\xi_1)^1$, $(\xi_2)^1$ and $(\xi_3)^1$. Since the three configurations should contribute equally to the $(t_{2g})^1$ state, it is necessary to consider the average spin-orbital interaction energy $\langle \Delta e \rangle$ defined elsewhere (35)

$$\langle \Delta e \rangle = \frac{1}{9} \sum_{\mu=1}^{3} \sum_{\nu=1}^{3} \Delta e_{\mu\nu}. \qquad [2]$$

If the orbitals ξ_1, ξ_2 and ξ_3 are symmetry-broken t_{2g}-orbitals, Eq. [2] consists of nine terms, i.e., six corner-sharing interactions and three edge-sharing interactions. For our rough estimation, it is reasonable to assume that the corner- and edge-sharing interaction are same in magnitude. Then from Eq. [2] we obtain

$$\Delta e_{\text{intra}} \approx \langle \Delta e \rangle. \qquad [3]$$

The $\langle \Delta e \rangle$ value can be determined by performing molecular orbital calculations for the intrachain spin dimer unit $(V_2S_9)^{10-}$, because in this case the orbitals ξ_1, ξ_2 and ξ_3 become symmetry-adapted t_{2g}-orbitals so that Eq. [2] becomes

$$\langle \Delta e \rangle = (\Delta e_{11} + \Delta e_{22} + \Delta e_{33})/9, \qquad [4]$$

where the Δe_{11}, Δe_{22} and Δe_{33} values refer to the energy separations between the bonding and the antibonding t_{2g}-block energy levels shown in Fig. 6. From Eqs. [2] and [4], the Δe_{intra} value is estimated as

$$\Delta e_{\text{intra}} \approx (\Delta e_{11} + \Delta e_{22} + \Delta e_{33})/9 \qquad [5]$$

Table 3 summarizes the results of our EHTB calculations of the spin-orbital interaction energies Δe_{inter} and Δe_{intra} for the 110, 60 and 5 K crystal structures of $BaVS_3$ (2). According to the relationship $J_{\text{AF}} \propto -(\Delta e)^2$, the interchain antiferromagnetic spin-exchange interaction is several times larger along the $(a + b)$-direction than along the a-direction. This is consistent with the observation that the antiferromagnetic ordering of $BaVS_3$ below ~ 30 K exhibits a spin ordering along the $(a + b)$-direction [7]. In addition, the antifer-

TABLE 3
Spin-Orbital Interaction Energies Δe_{inter} and Δe_{intra} (in meV) Calculated for the 110, 60 and 5 K Crystal Structures of $BaVS_3$

	100 K	60 K	5 K
Δe_{inter} [$//(a + b)$]	215	248	227
Δe_{inter} [$//a$]	127	103	112
Δe_{intra} [$//c$]	108	104	101

romagnetic spin-exchange interaction is several times smaller along the chain than along the $(a + b)$ interchain direction. It should be noted that a spin-exchange parameter is given by $J = J_F + J_{AF}$. Unlike the case of super–super-exchange interactions, the J_F term is not always negligible for super-exchange interactions because J_F depends on the overlap density between magnetic orbitals (17). This might explain why the intrachain spin-exchange interaction is ferromagnetic in $BaVS_3$ below ~ 30 K.

Consequently, the preferential antiferromagnetic spin-exchange interactions along the interchain direction in $BaVS_3$ can be easily understood if the magnetic orbitals of $BaVS_3$ are represented by the symmetry-broken t_{2g}-orbitals rather than by symmetry-adapted t_{2g}-orbitals. To understand why this is the case, we consider the orbital interaction in a spin dimer in more detail (Fig. 4a). Since the two sites are chemically equivalent, their magnetic orbitals χ_1 and χ_2 are the same in energy (i.e., e_1^0). The interaction between the two orbitals gives rise to the bonding level ϕ_1 with energy e_1 and the antibonding level ϕ_2 with energy e_2 such that $(e_2 - e_1^0) > (e_1^0 - e_1)$ (36). For a spin dimer, the on-site repulsion is large so that the orbitals ϕ_1 and ϕ_2 are both singly occupied (Fig. 4c) (18). Thus the net result of the orbital interaction is destabilization, i.e., $\Delta E = (e_2 + e_1) - 2e_1^0 \propto (S_{12})^2 > 0$ (36). This destabilization is reduced if the orbitals χ_1 and χ_2 can be so arranged to decrease S_{12}. When the symmetry-adapted t_{2g}-orbitals are used, the Δe_{intra} value becomes very large. For example, when the $3z^2$–r^2 orbitals become magnetic orbitals (Fig. 19d), the Δe_{intra} value is calculated to be 622 meV. Thus, the preference for the symmetry-broken t_{2g}-orbitals in the magnetic insulating state of $BaVS_3$ can be rationalized as a consequence of minimizing destabilizing orbital interactions ΔE. As discussed already (37), the cooperative Jahn–Teller distortion and orbital/spin ordering phenomena of magnetic solids are explained as a consequence of minimizing such destabilizing orbital interactions.

5. CONCLUDING REMARKS

$BaVS_3$ is made up of individual VS_3 octahedral chains but its electrical conductivity is nearly isotropic due to the orbital interactions associated with the short intrachain and interchain S ⋯ S contacts. In the metallic state, the $3z^2$–r^2 band is partially filled and should contribute to the electrical conductivity mainly along the chain direction. The conductivity along the interchain directions should be related to the narrow bands that give rise to the sharp DOS peak lying at the Fermi level. Our first principles electronic structure calculations indicate that the metallic and magnetic insulating states of $BaVS_3$ should be nearly identical in stability, in support of the experimental finding that electron localization is responsible for the metal–insulator transition at ~ 70 K. The magnetic properties of $BaVS_3$ below ~ 70 K are well accounted for if the symmetry-broken t_{2g}-orbitals are regarded as the magnetic orbitals in the magnetic insulating state of $BaVS_3$. The latter is probable because the symmetry-broken t_{2g}-orbitals minimize the destabilizing two-electron two-orbital interactions.

ACKNOWLEDGMENTS

The work at North Carolina State University was supported by the Office of Basic Energy Sciences, Division of Materials Sciences, U. S. Department of Energy, under Grant DE-FG02-86ER45259. The computational work at ICMCB was aided by the M3PEC project (Modélisation Microscopique et Mésoscopique en Physique, dans l'Environnement et en Chimie), Université de Bordeaux I.

REFERENCES

1. R. A. Gardner, M. Vlasse, and A. Wold, *Acta Crystallogr. B* **25,** 781 (1969).
2. M. Ghedira, M. Anne, J. Chenavas, M. Marezio, and F. Sayetat, *J. Phys. C: Solid State Phys.* **19,** 6489 (1986), and the papers cited therein.
3. M. Nakamura, A. Sekiyama, H. Namatame, A. Fujimori, H. Yoshihara, T. Ohtani, A. Misu, and M. Takano, *Phys. Rev. B* **49,** 16191 (1994), and the references cited therein.
4. T. Graf, D. Mandrus, J. M. Lawrence, J. D. Thompson, and P. C. Canfield, *Phys. Rev. B* **51,** 2037 (1995).
5. H. Nakamura, H. Imai, and M. Shiga, *Phys. Rev. Lett.* **79,** 3779 (1997).
6. G. Mihály, I. Kézsmárki, F. Zámborsky, M. Miljak, K. Penc, P. Fazekas, H. Berger, and L. Forró, *Phys. Rev. B* **61,** R7831 (2000).
7. H. Nakamura, T. Yamasaki, S. Giri, H. Imai, M. Shiga, K. Kojima, M. Hishi, K. Kakurai, and N. Metoki, *J. Phys. Soc. Jpn.* **69,** 2763 (2000).
8. I. Kézsmárki, Sz. Csonka, H. Berger, L. Forró, P. Fazekas, and G. Mihály, *Phys. Rev. B* **63,** 081106(R) (2001).
9. M. Shiga, H. Imai, H. Mitamura, and T. Goto, *Physica B* **294–295,** 149 (2001).
10. L. F. Mattheiss, *Solid State Commun.* **93,** 791 (1995).
11. H. Imai, H. Wada, and M. Shiga, *J. Phys. Soc. Jpn.* **65,** 791 (1996).
12. H. Nakamura, H. Tanahashi, H. Imai, M. Shiga, K. Kojima, K. Kakurai, and M. Nishi, *J. Phys. Chem. Solids* **61,** 1137 (1999).
13. M.-H. Whangbo, M. J. Foshee, and R. Hoffmann, *Inorg. Chem.* **19,** 1723 (1980).
14. O. Kahn, "Molecular Magnetism," VCH Publishers, Weinheim, 1993.
15. H.-J. Koo and M.-H. Whangbo, *J. Solid State Chem.* **153,** 263 (2000).
16. H.-J. Koo and M.-H. Whangbo, *Inorg. Chem.* **39,** 3599 (2000).
17. H.-J. Koo and M.-H. Whangbo, *Inorg. Chem.* **40,** 2169 (2001).
18. M.-H. Whangbo, *J. Chem. Phys.* **70,** 4963 (1979).
19. N. F. Mott, "Metal-Insulator Transitions," 2nd Ed. Taylor and Francis, New York, 1990.
20. Amsterdam Density Functional (ADF2.01) Program, Theoretical Chemistry, Vrije Universiteit, Amsterdam, 1995.
21. S. H. Vosko, L. Wilk, and M. Nusair, *Can. J. Phys.* **58,** 1200 (1980).
22. A. D. Becke, *Phys. Rev. A* **38,** 3098 (1988).
23. J. P. Perdew, *Phys. Rev. B* **33,** 8822 (1986).
24. V. I. Anisimov, F. Aryasetiawan, and A. I. Lichtenstein, *J. Phys.: Condens. Matter* **9,** 767 (1997), and the references cited therein.
25. P. Blaha, K. Schwarz, and J. Luitz, WIEN97, Vienna University of Technology 1997. (Improved and updated version of the original copyrighted WIEN-code. See: P. Blaha, K. Schwarz, P. Sorantin, and S. B. Trickey, *Comp. Phys. Commun.* **59,** 399 (1990)).

26. J. P. Perdew, S. Burke, and M. Ernzerhof, *Phys. Rev. Lett*. **77,** 3865 (1996).
27. M.-H. Whangbo, *Inorg. Chem.* **19,** 1728 (1980).
28. M.-H. Whangbo, H.-J. Koo, A. Villesuzanne, and M. Pouchard, *Inorg. Chem*., in press.
29. M.-H. Whangbo and R. Hoffmann, *J. Am. Chem. Soc*. **100,** 6093 (1978).
30. Our calculations were carried out by employing the *CAESAR* program package (J. Ren, W. Liang, and M.-H. Whangbo, *Crystal and Electronic Structure Analysis Using CAESAR*, 1998, *http://www.PrimeC.com/*.)
31. E. Clementi and C. Roetti, *At. Data Nucl. Data Tables*, **14,** 177 (1974).
32. J. M. Williams, H. H. Wang, T. J. Emge, U. Geiser, M. A. Beno, P. C. W. Leung, K. D. Carlson, R. J. Thorn, A. J. Schultz, and M.-H. Whangbo, *Prog. Inorg. Chem.* **35,** 51 (1987).
33. M.-H. Whangbo and E. Canadell, *J. Am. Chem. Soc*. **114,** 9587 (1992).
34. O. Gourdon, M. Evain, S. Jobic, R. Brec, H.-J. Koo, M.-H. Whangbo, B. Corraze, and O. Chauvet, *Inorg. Chem.* **40,** 2898 (2001).
35. M.-H. Whangbo, H.-J. Koo, M. A. Continentino, and J. Dumas, *Inorg. Chem*., in press.
36. T. A. Albright, J. K. Burdett, and M.-H. Whangbo, "Orbital Inetractions in Chemistry." Wiley, New York, 1985.
37. M.-H. Whangbo and H.-J. Koo, *Solid State Sci*., in press.